First results from the rapid-response spectrophotometric characterization of Near-Earth Objects using RATIR

S. Navarro-Meza,[1,2] M. Mommert,[3,2] D.E. Trilling,[2] N. Butler,[4,5] M. Reyes-Ruiz,[1] B. Pichardo,[6] T. Axelrod,[7] R. Jedicke,[8] and N. Moskovitz[3]

[1]*Instituto de Astronomía, Universidad Nacional Autónoma de México, Ensenada B.C. 22860, México.*

[2]*Department of Physics and Astronomy, Northern Arizona University, Flagstaff, AZ 86001, USA*

[3]*Lowell Observatory, Flagstaff, AZ 86001, USA*

[4]*School of Earth and Space exploration, Arizona State University, Tempe, AZ 85287, USA*

[5]*Cosmology Initiative, Arizona State University, Tempe, AZ 85287, USA*

[6]*Instituto de Astronomía, Universidad Nacional Autónoma de México, Ciudad Universitaria, D.F. 04510, México.*

[7]*Steward Observatory, University of Arizona, Tucson, AZ 85721, USA*

[8]*Institute for Astronomy, University of Hawaii at Manoa, Honolulu, HI 96822, USA*

ABSTRACT

As part of our multi-observatory, multi-filter campaign, we present r-i color observations of 82 Near-Earth Objects (NEOs) obtained with the RATIR instrument on the 1.5 m robotic telescope at the San Pedro Martir's National Observatory in Mexico. Our project is particularly focused on rapid response observations of small ($\lesssim 850$ m) NEOs. The rapid response and the use of spectrophotometry allows us to constrain the taxonomic classification of NEOs with high efficiency. Here we present the methodology of our observations and our result, suggesting that the ratio of C-type to S-type asteroids

Corresponding author: S. Navarro-Meza
snavarro@astro.unam.mx

in a size range of ∼30-850m is 1.1, which is in accordance with our previous results.
We also find that 10% of all NEOs in our sample are neither C- nor S-type asteroids

Keywords: asteroids: individual (near-Earth objects) — minor planets — surveys

1. INTRODUCTION

Solar System minor bodies are tracers of the Solar System's formation and evolution, and hence can be used as current samples of the processes that occurred in the early days of the system and its formation (Delsemme 1991; Malhotra 1997). Therefore, studies with numerous samples, focused on analyzing colors, taxonomies, orbital and physical properties of asteroids from different populations have been made (see for example Ivezić et al. 2001; Carvano et al. 2010; Carry et al. 2016).

Near Earth Objects (NEOs) are of particular interest for their potential to explain the disagreement between the composition of meteorite falls on Earth and the composition observed in asteroids (Mommert et al. 2016). Furthermore, the Chelyabinsk event in 2013 showed us that there exist NEOs with the potential to cause moderate to devastating damage to our communities (Brown et al. 2013). It is worth to remark that events like this can happen in any point on the globe. This event has motivated projects aimed to characterize those asteroids that could impact the Earth and that have enough energy to compromise its safety.

Discovery and characterization efforts aimed at NEOs have significantly increased in the last years. However, due to their general faintness, characterization of small NEOs lags behind. The most effective way to constrain NEO compositions is spectroscopy, which allows for the identification of both the overall continuum shape and diagnostic band features and enables their taxonomic classification. However, spectroscopy is very expensive in terms of telescope time, and is only possible with relatively bright objects, which generally are the largest objects. Only few small asteroids (with diameters smaller than 100 m) get bright enough to be observed spectroscopically (e.g. Moskovitz et

al. 2015). Currently, DeMeo et al. (2009) offer the most complete taxonomic classification system.

Photometric measurements at a few key wavelengths -*spectrophotometry*- can be sufficient to estimate asteroid taxonomies (see Mommert et al. 2016, and references therein). This technique has the advantage of making faint targets accessible because the light is collected within a broad bandpass instead of being dispersed as a function of wavelength. Furthermore, spectrophotometry can be performed with smaller telescopes than the ones necessary for spectroscopy. Here we present a combination of spectrophotometry and *rapid-response* observations, i.e., observations that are obtained shortly after the discovery of the target, when it is still relatively bright. This article constitutes the third of a series of papers oriented to taxonomically classify hundreds of small NEOs using spectrophotometry.

C- (organic rich) and S- (siliceous rock) taxonomic types are the dominant constituents of the distribution of large asteroids (Stuart & Binzel 2004; Thomas et al. 2011). However, the compositional distribution of small NEOs appears to be different from that of Main Belt asteroids, as well as from large NEOs. Mommert et al. (2016) find S and C+X[1] complexes to be the main components of their sample of small NEOs. Also as pointed out by them, the compositional distribution of meteorite falls does not match the observed NEO distribution, a fact that can yield information on asteroid strength. This fact needs to be studied with better statistics on the small asteroid range in order to better understand the threat to Earth from impactors. It is important to remark that according to Thomas et al. (2011, 2014), Q-type asteroids can be an important component of a magnitude biased NEO sample, due to their relatively high albedos. There are other teams interested in this same topic (see for example Popescu et al. 2018; Ieva et al. 2018).

[1] Results from Mommert et al. (2016) make no distinction between the C and the X taxonomic complexes. For comparison purposes the notation C+X will be used here, which stands for the set of objects corresponding to both, the C and the X complexes.

This study is part of a worldwide systematic survey of NEO compositions. With the use of the 3.8 m United Kingdom Infrared Telescope (UKIRT) and KMTNet-SAAO telescope, we provide detailed information on the compositional distribution of NEOs with absolute magnitudes up to $H \sim 28$, i.e., with a few meters in diameter. Such rapid response is generally not feasible through classical observing proposals due to heavily oversubscribed classicaly scheduled major research facilities. Furthermore, this method allows us to classify small NEOs according to their taxonomy with a higher efficiency than current spectroscopic methods (see Galache et al. 2015 for a discussion). Furthermore, photometric studies of the partial lightcurves of our objects can lead to improve the period distribution of asteroids on the smaller range (see Warner et al. 2009).

In Section 2 we describe RATIR, the multiband instrument we use. Section 3 describes our rapid response approach and the planing of our observations. Section 4 addresses our data selection and analysis. In Section 5 we provide our results and the corresponding discussion is given in 6. Finally in Section 7 we discuss the conclusions and the future outlook of this project.

2. RATIR

Observations were performed with the Reionization And Transients InfraRed camera (RATIR, Butler et al. 2012), on the San Pedro Martir (SPM) 1.5 m telescope at the National Mexican Astronomical Observatory (Observatorio Astronómico Nacional). This telescope is a Ritchey-Chrétien type, operated by the Universidad Nacional Autónoma de México. The instrument is equipped with two optical and two near-infrared (NIR) detectors, all of them 2048x2048 pixels. Each of these detectors corresponds to a different channel with specific filters, as shown in Table 1. RATIR takes four images of an object in a single shot[2] . To minimize dark current and thermal background effects, the optical detectors are water cooled, while the NIR detectors are operated in a helium-cooled cryostat.

---

[2] See detailed information in RATIR's web page: http://ratir.astroscu.unam.mx

Channel	Detector	Field size	Filters
		(arc minute square)	
C0	CCD	5.3	SDSS ugr and seven others
C1	CCD	5.3	Fixed SDSS i
C2	H2RG	10	Fixed WFCAM Z and Y
C3	H2RG	10	Fixed MKO J and H

Table 1. Channels of the RATIR instrument. All detectors are 2048x2048 pixels. C0 and C1 channels hold the visual range filters (observations reported in this paper were taken with the r and i filters). C2 and C3 channels contain the near infrared filters; H2RG (HAWAII-2RG) are Teledyne mercury-cadmium-telluride detectors.

RATIR was designed to study gamma ray bursts (e.g. Butler et al. 2017a,b,c), but other uses are possible as shown here (see also Tapia et al. 2014; García-Díaz et al. 2014; Ricci et al. 2015). Observations are executed in an automated queue mode (Watson et al. 2012) if no gamma ray burst events are ongoing. The results that we present are the first asteroid observations made with the instrument.

3. OBSERVATIONS

The observations we present here were taken during 2014 and 2015. During most part of 2015 and 2016, RATIR's channels C2 and C3 (see Table 1) were not available due to technical problems. In this work, we analyze the set of optical-only data. Since the second half of 2016 we are obtaining observations in all four channels, which will be presented in a future publication.

Our rapid response approach is the key feature of this project. We trigger rapid response spectrophotometric observations of NEOs within a few days of their discovery when the objects are generally still bright enough to be observed with a 1.5 m aperture. We can observe and characterize objects as faint as V $\sim$ 20. Such rapid response is generally not feasible through classical observing

programs. The first results of NEO observations made by our team are presented in Mommert et al. (2016) and Erasmus et al. (2017).

Potential targets are identified and uploaded into the RATIR queue on a daily basis. Accessible targets are identified among those NEOs that have been discovered within the last four weeks; this duration is partially arbitrary[3], but the method usually leads to a number of well-observable and bright potential targets. A target is considered accessible if it has a visible brightness $V \leq 20$ and an air-mass ≤ 2.0, as provided by the JPL Horizons system (Giorgini et al. 1997), for at least the duration of the estimated RATIR integration time. Potential targets are manually selected from the list of accessible targets, prioritizing objects with high absolute magnitudes H_V (small sizes) and large values of H_V -V, where V stands for the apparent magnitude of the target of the upcoming night. A high value of H_V -V ensures that our target is observed when it is close to the Earth. RATIR queue observing scripts are automatically created for the selected targets, using the latest orbital elements of the objects of interest provided by JPL Horizons. The exposure time of each frame, as well as the total integration time in each band per visit are a function of the object's brightness. Exposure times usually ranges between 5 and 30 seconds, while the total integration time per target is usually less than 1 hour.

Our observations are biased in favor of bright objects. At a given distance from Earth, for objects of a given diameter, objects with higher albedo are easier to observe. For targets close to our limiting magnitude, only those with relatively high albedos will be observed. Hence, our sample may contain a higher fraction of S and Q objects than the actual asteroid population.

4. DATA ANALYSIS

---

[3] After the closest approach, NEOs fade at a rate of typically 0.5 mag within one week and 5 mag within 6 weeks (Galache et al. 2015).

Object	Obs. Midtime (UT)	Dur. (hr)	H_V (mag)	r-i (mag)	error (mag)
2014 MK6	2014-07-22 09:30	1.7	21.00	0.29	0.01
2014 MP5	2014-07-21 05:25	1.5	21.80	0.27	0.02
2014 OZ337	2014-08-04 08:13	0.3	22.50	0.35	0.02
2014 QQ33	2014-08-25 10:20	1.3	22.10	0.30	0.02
2014 TT35	2014-10-18 03:49	0.1	26.00	0.49	0.01
2014 TZ	2014-10-23 05:12	1.1	22.60	0.33	0.01
2014 UT192	2014-11-10 09:03	0.2	19.60	0.46	0.03
2014 UZ116	2014-11-03 06:41	1.6	20.90	0.36	0.04
2014 WX4	2014-11-20 07:16	0.5	26.40	0.40	0.02
2014 WZ4	2014-11-20 03:42	0.5	23.50	0.29	0.03
2014 YE35	2015-01-15 08:32	0.5	20.30	0.38	0.01
2014 YW34	2015-01-15 06:53	1.6	21.60	0.25	0.06
2015 EL7	2015-04-05 10:19	0.4	22.70	0.38	0.03
2015 EL7	2015-04-09 07:40	0.2	22.70	0.39	0.06
2015 EL7	2015-04-11 07:22	0.1	22.70	0.36	0.03
2015 EZ	2015-03-15 05:56	0.4	20.30	0.40	0.01
2015 FG120	2015-04-10 09:12	1.1	22.90	0.36	0.02
2015 FG120	2015-04-11 09:20	0.2	22.90	0.29	0.03
2015 FG120	2015-04-12 09:35	1.0	22.90	0.30	0.02
2015 FG120	2015-04-13 08:07	0.9	22.90	0.38	0.02
2015 FG120	2015-04-17 11:09	0.7	22.90	0.37	0.02
2015 FG37	2015-04-15 10:53	1.1	21.70	0.41	0.02
2015 FG37	2015-04-22 11:25	0.1	21.70	0.29	0.04
2015 FL290	2015-04-09 05:11	1.1	22.20	0.36	0.02
2015 FL290	2015-04-10 04:53	1.1	22.20	0.37	0.02
2015 FL290	2015-04-11 04:46	1.2	22.20	0.39	0.01

Table 2. This table presents each of the reported targets according to their number or designation, observation midtime of the observing run, and the duration of it. Also presented are, the measured color indices (solar colors have been subtracted) and corresponding uncertainties.

Object	Obs. Midtime	Dur.	H_V	r-i	error
	(UT)	(hr)	(mag)	(mag)	(mag)
2015 FQ	2015-03-29 05:43	0.9	22.30	0.40	0.02
2015 FT118	2015-04-20 10:50	0.6	20.40	0.30	0.04
2015 FY284	2015-04-02 07:13	0.5	21.60	0.37	0.05
2015 GS13	2015-05-14 09:26	0.4	21.00	0.51	0.03
2015 GS	2015-04-15 09:34	1.1	20.60	0.35	0.02
2015 GS	2015-04-16 09:53	1.2	20.60	0.33	0.02
2015 GY	2015-04-15 05:14	0.6	21.70	0.41	0.01
2015 GY	2015-04-19 07:16	0.5	21.70	0.27	0.02
2015 HA1	2015-04-25 09:04	0.9	21.20	0.46	0.01
2015 HA1	2015-05-05 07:50	0.5	21.20	0.45	0.01
2015 HP171	2015-05-12 09:32	0.3	20.10	0.34	0.02
2015 HR1	2015-05-06 08:59	0.7	24.30	0.35	0.06
2015 HR1	2015-05-07 09:00	0.4	24.30	0.34	0.06
2015 HR1	2015-05-13 09:39	0.7	24.30	0.26	0.03
2015 HV171	2015-05-08 08:55	0.1	18.10	0.36	0.01
2015 HW11	2015-05-12 07:04	1.1	23.30	0.41	0.02
2015 JQ1	2015-05-18 05:03	1.0	20.30	0.26	0.05
2015 JQ1	2015-05-19 05:45	1.0	20.30	0.28	0.02
2015 KL122	2015-06-05 09:19	0.5	22.30	0.47	0.07
2015 KQ120	2015-05-30 10:10	0.1	26.70	0.43	0.04
2015 KQ57	2015-05-26 05:17	0.0	22.20	0.40	0.04
2015 KV18	2015-05-23 09:41	0.8	23.80	0.42	0.03
2015 KV18	2015-05-24 09:28	0.8	23.80	0.37	0.04
2015 KV18	2015-05-25 07:40	0.2	23.80	0.31	0.02
2015 KV18	2015-05-26 07:40	0.1	23.80	0.41	0.03
2015 LA2	2015-06-14 06:35	1.0	23.10	0.33	0.01
2015 LG14	2015-06-22 06:22	1.0	23.20	0.40	0.03
2015 LG14	2015-06-23 06:03	0.8	23.20	0.52	0.04
2015 LG2	2015-06-18 07:18	1.0	20.30	0.40	0.03

Table 2. (continued).

Object	Obs. Midtime (UT)	Dur. (hr)	H_V (mag)	$r-i$ (mag)	error (mag)
2015 LG2	2015-06-21 08:41	0.8	20.30	0.37	0.02
2015 LJ24	2015-06-18 05:11	0.2	20.00	0.42	0.03
2015 LJ	2015-07-04 06:43	0.8	24.70	0.45	0.05
2015 LJ	2015-07-04 07:50	0.8	24.70	0.33	0.07
2015 LJ	2015-07-13 05:21	0.8	24.70	0.27	0.03
2015 LJ	2015-07-25 06:54	0.9	24.70	0.29	0.06
2015 LQ21	2015-06-21 05:01	0.1	24.50	0.50	0.03
2015 MC	2015-06-20 06:18	0.2	24.10	0.45	0.02
2015 MC	2015-06-26 06:49	0.9	24.10	0.30	0.04
2015 ME116	2015-07-14 04:57	0.3	22.30	0.38	0.06
2015 ME116	2015-07-25 04:49	0.4	22.30	0.27	0.04
2015 MQ116	2015-07-15 08:09	0.8	23.40	0.35	0.05
2015 MS59	2015-07-13 10:15	0.9	21.00	0.25	0.01
2015 MS59	2015-07-14 09:26	0.9	21.00	0.49	0.02
2015 MS59	2015-07-15 09:25	1.0	21.00	0.41	0.02
2015 MS59	2015-07-23 09:48	0.9	21.00	0.37	0.04
2015 MU59	2015-07-09 10:01	0.8	20.00	0.31	0.02
2015 MU59	2015-07-13 09:15	0.8	20.00	0.44	0.01
2015 MU59	2015-08-04 08:44	0.6	20.00	0.39	0.01
2015 MX103	2015-07-04 05:13	0.5	24.40	0.46	0.02
2015 MX103	2015-07-06 06:16	0.6	24.40	0.38	0.02
2015 MY53	2015-07-03 05:59	0.5	25.40	0.39	0.06
2015 MY53	2015-07-03 06:49	0.2	25.40	0.52	0.03
2015 NK13	2015-08-04 07:07	0.8	21.00	0.40	0.03
2015 NK3	2015-08-04 05:56	0.8	21.30	0.26	0.03
2015 NK3	2015-08-07 06:57	1.0	21.30	0.28	0.01
2015 NU2	2015-07-21 07:10	0.6	20.90	0.28	0.04
2015 NU2	2015-07-24 05:15	1.1	20.90	0.35	0.04

Table 2. (continued)

Object	Obs. Midtime	Dur.	H_V	r-i	error
	(UT)	(hr)	(mag)	(mag)	(mag)
2015 OF26	2015-08-07 05:37	0.3	21.60	0.32	0.02
2015 OM21	2015-07-24 09:55	0.7	22.50	0.38	0.03
2015 OM21	2015-08-06 08:00	0.9	22.50	0.45	0.03
2015 OM21	2015-08-07 08:05	1.0	22.50	0.48	0.02
2015 PA229	2015-08-21 09:39	1.0	21.40	0.41	0.02
2015 PA229	2015-09-05 08:55	1.0	21.40	0.39	0.05
2015 PQ56	2015-09-03 07:59	0.9	22.60	0.46	0.04
2015 PQ	2015-09-07 07:52	0.7	22.70	0.48	0.01
2015 QB	2015-08-21 08:32	1.0	24.20	0.39	0.01
2015 QG	2015-08-22 05:17	0.3	23.80	0.33	0.02
2015 QM3	2015-08-23 04:45	0.4	20.40	0.28	0.05
2015 QN3	2015-08-23 04:20	0.4	19.50	0.28	0.01
2015 QN3	2015-08-24 04:56	0.4	19.50	0.40	0.01
2015 QO3	2015-08-24 07:05	0.6	19.40	0.38	0.01
2015 RH36	2015-09-18 09:57	0.5	23.60	0.37	0.06
2015 RO36	2015-09-18 05:36	0.3	22.90	0.24	0.03
2015 RQ36	2015-09-16 07:25	1.0	24.50	0.36	0.01
2015 RQ36	2015-09-19 09:05	0.6	24.50	0.35	0.02
2015 SO2	2015-09-26 09:01	0.3	23.90	0.37	0.03
2015 SO2	2015-09-27 09:33	0.3	23.90	0.29	0.03
2015 SO2	2015-09-28 10:57	0.3	23.90	0.50	0.03
2015 SO2	2015-10-02 11:21	0.4	23.90	0.32	0.03
2015 SV2	2015-09-29 05:31	0.9	20.80	0.33	0.03
2015 SY	2015-10-01 06:35	0.7	23.30	0.44	0.02
2015 SY	2015-10-02 06:09	0.8	23.30	0.33	0.03
2015 SZ	2015-10-02 05:22	0.4	23.50	0.36	0.01
2015 TE	2015-10-08 04:26	0.5	22.50	0.43	0.02

Table 2. (continued)

Object	Obs. Midtime	Dur.	H_{V}	r-i	error
	(UT)	(hr)	(mag)	(mag)	(mag)
2015 TF	2015-10-10 05:15	0.6	22.20	0.39	0.01
2015 TW178	2015-10-26 04:18	0.9	21.20	0.28	0.04
2015 TY144	2015-10-26 10:14	0.5	21.30	0.48	0.05
2015 TY178	2015-11-06 06:52	0.7	21.80	0.32	0.04
2015 UJ51	2015-10-27 07:41	0.7	21.40	0.38	0.03
2015 US51	2015-10-28 04:54	0.6	22.40	0.44	0.02
2015 US51	2015-11-01 05:02	0.8	22.40	0.43	0.01
2015 US51	2015-11-02 04:35	0.8	22.40	0.44	0.01
2015 UT52	2015-11-05 07:40	0.8	20.90	0.45	0.03
2015 UT52	2015-11-11 10:56	0.6	20.90	0.40	0.04
2015 VJ2	2015-11-10 09:36	0.4	19.60	0.44	0.02
2015 VJ2	2015-11-18 10:50	0.2	19.60	0.37	0.03
2015 VJ2	2015-11-19 10:06	0.6	19.60	0.26	0.01
2015 VO66	2015-11-14 10:06	0.4	20.60	0.25	0.03
2015 VO66	2015-11-19 08:20	0.5	20.60	0.28	0.01
2015 VZ2	2015-11-19 04:15	0.9	22.70	0.46	0.04
2014 OT338	2014-08-17 11:10	1.4	21.40	0.45	0.02
2014 TX32	2014-10-16 05:35	1.1	20.20	0.42	0.01
2015 DE176	2015-02-28 06:18	1.0	19.70	0.35	0.03
2015 JV	2015-05-19 07:35	0.8	21.50	0.33	0.01
2015 KJ19	2015-05-24 04:53	0.6	22.50	0.28	0.07

Table 2. (continued)

4.1. *Taxonomic classification*

We use the Bus-DeMeo classification scheme (DeMeo et al. 2009) to classify our sample. This is a widely used taxonomic scheme that combines the visible and near infrared ranges, covering from
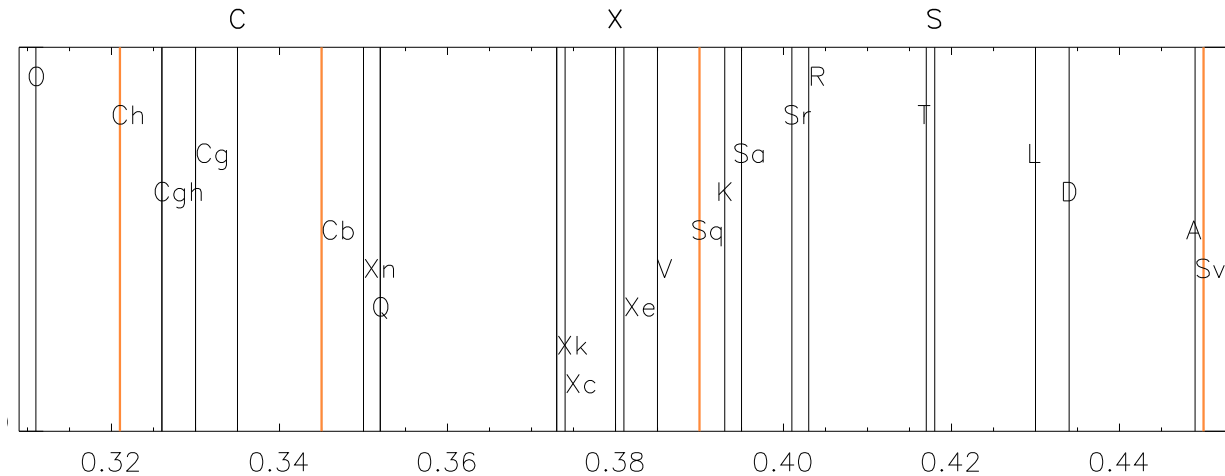
Figure 1. All r-i indices considered in this work according to the Bus-DeMeo taxonomies. Orange lines are the subtypes that are most distant from the C- and S-type respectively, thus defining the limits of these complexes . Notice that the C- and S-subtype are in the middle of their complexes.

0.45 to 2.45 μm. The taxonomy includes 24 classes, most of which correspond to the C-, S- and X-complexes that include the majority of the known asteroids (see DeMeo et al. 2009, and Section 1). For this reason, we considered these 3 complexes in our analysis, as well as the Q-type, which, as described by Thomas et al. (2011, 2014), can be an important component of a magnitude biased NEO sample like ours. Other taxonomic types were not considered, as they are not expected to be a significant part of the distribution (perhaps up to 20%: Mommert et al. (2016); Erasmus et al. (2017); Perna et al. (2018); Lin et al. (2018)) and due to the simplicity of our model. We revisit this assumption below.

We obtain the characteristic color of each taxonomic type from a sample of measured asteroid spectra[4]. For each object from the sample, its reflectance spectrum is convolved with the spectral response of each RATIR's filter and the solar spectrum. Details of the process can be found at

---

[4] http://smass.mit.edu/minus.html

Mommert et al. (2016), Section 3. Figure 1 shows these color indices in the r-i color.

4.2. *Photometry*

Image reduction and photometry is carried out using a pipeline developed for GRB observations (see, e.g. Becerra et al. 2017; Littlejohns et al. 2015). Briefly, the pipeline reduces, sky-subtracts, and aligns input frames. These frames are then stacked into a sky image. The stellar PSF is determined and fit using custom python scripts to determine the photometric zero point in comparison with SDSS, 2MASS, and/or USNO photometric catalogs. After finishing the GRB pipeline reduction, we create a source mask using the sky image. By then coadding the frames in the moving frame of the target, keeping track of the exposure per pixel, the non-moving sources are removed and we retain only the signal from the target. The PSF determined from the sky image is then fit to the moving-target image and the zero point from the sky image is applied to normalize the photometry.

The magnitude of an object as a function of the observing time is generated by dyadically combining the masked frames, selecting a sufficiently long time interval for each photometric epoch as to adequately fill in masked pixels prior to PSF fitting. In principle, single frame photometry is possible because we propagate the exposure pixel by pixel; however the accuracy can depend strongly on the stability of the PSF.

Therefore, the pipeline yields photometry on the original image, on a set of stacked images, and on the overall visit's stacked frame. The stacking creates new images with different virtual exposure times which are integer multiples of the real exposure time. The result of this procedure is available in data tables and through a graphical display in a website. In our analysis we use the photometry measured in individual r band and i band images. With this information we measure the r-i color index. The Solar r-i was subtracted from our measurements in order to make them compatible with the synthetized colors (see Section 4.1).

4.3. *Outlier rejection*

In order to reject photometric outliers we performed a $10 - \sigma$ clipping on the r-i index for each visit: a weighted mean of the r-i index was taken, then any measurement further than 10σ from the mean was rejected and the weighted mean calculated again. This process was carried out 3 times. Each time the photometric errors from the individual measurements were propagated to obtain the weights (Taylor 1997). Therefore, the corresponding error on the r-i index from a visit is:

$$\varsigma = \frac{1}{\sqrt{\Sigma w_{\mathrm{k}}}}, \tag{1}$$

where

$$w_{\mathrm{k}} = \frac{1}{e_{\mathrm{k}}^2} \equiv \frac{1}{e_r^2 + e_i^2} \tag{2}$$

where e_{k} is associated with the r-i from each of the non-rejected data points of that visit and e_r and e_i are the photometric errors from the r and i band measurements. The values of ς are plotted in Figure 2.

4.4. *Selection of the best observations*

We only consider measurements of those objects that passed through all of our selection criteria, the first of which is a clean visit-stacked image: a well defined source and a successful removal of the not moving sources (see Section 4.2 for details on the photometry). Note that we use the visit stacked image only to check the quality of the photometry and of the observation itself, e.g., with respect to background sources confusion. Also, a limit on the color index's error due to photometric uncertainty must be set. The difference in color index between the C- and S-type asteroids is 0.084, hence it is convenient that we only consider the objects that have an error lower than this threshold. Based on the discussion on Section 6.2, we decide to use 0.075 as an upper error limit on the color determination. We require a minimum of 4 measurements per visit.
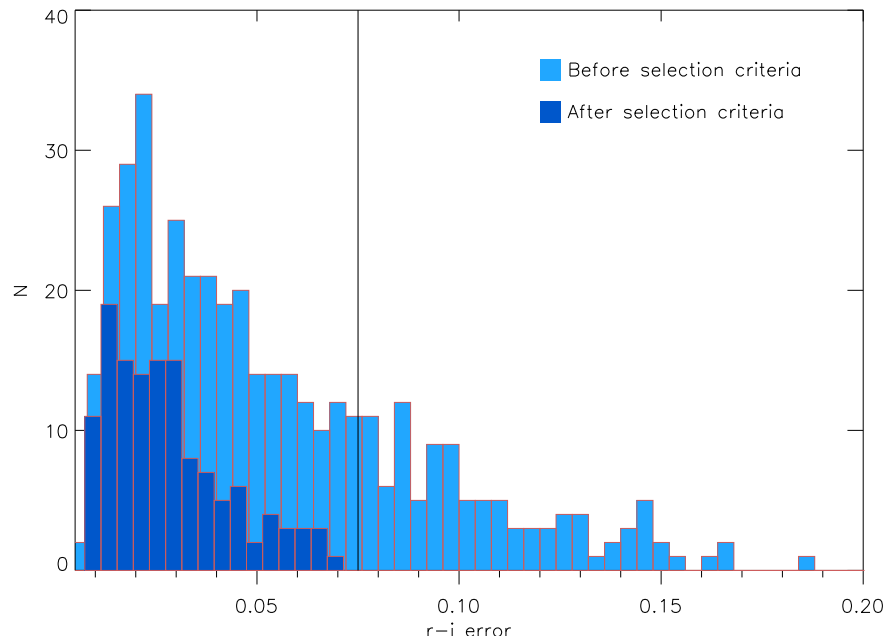
Figure 2. Error distribution of the color from our sample. The vertical line shows the upper error limit set for the sample. See Section 4.4 for details on the selection criteria used.

The outcome of this selection process is 82 different objects observed in 131 visits.

4.5. *Probability density*

After the selection process described in the previous section, we have one r-i index and its associated error for each visit in our clean sample. These indices are shown in Figure 3. In order to analyze the taxonomic distribution of our sample, we model it based on the known asteroid colors. We consider every count in Figure 3 as a normalized Gaussian centered at the r-i value of that object with the width of the Gaussian equal to the error on the r-i index (the height is therefore a free parameter). For objects observed more than once, the Gaussian's normalization factor is divided by the number of visits each object has. That way an object observed in more than one visit will be represented by different Gaussians all of which add up an area of unity. The Gaussians corresponding to all objects were added up to obtain the Probability Density Function (PDF), shown in Figure 4.
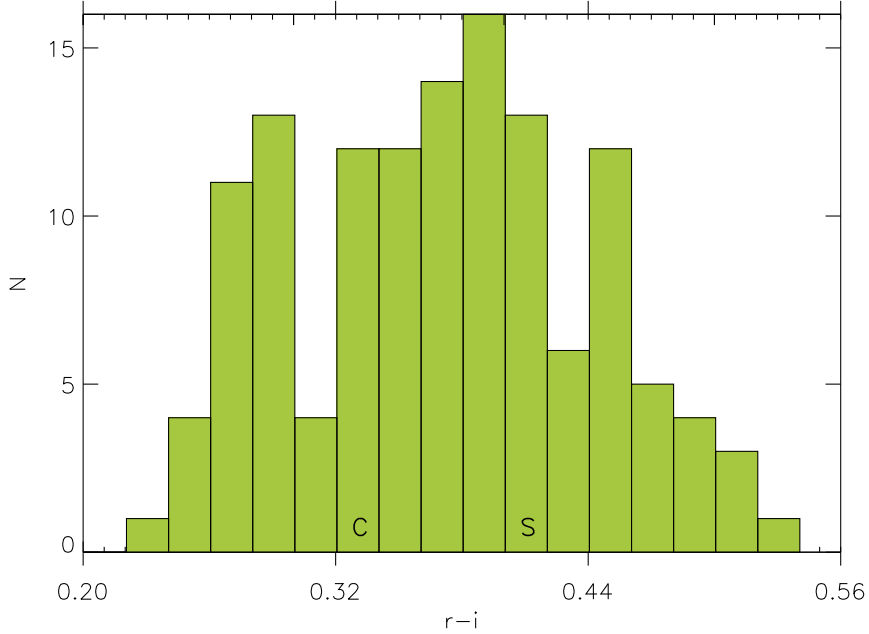
Figure 3. Color distribution of our sample. Color indices were obtained after performing the rejection process described in the text. The main subtypes from the C- and S-complex are shown (see Figure 1).

4.6. *Monte Carlo simulation*

In order to measure the compositional distribution from the PDF, we conducted a Monte Carlo (MC) simulation, which consists of creating 10^7 samples of synthetic asteroids, each sample with the same number of objects as our data sample but with different taxonomic distributions. In each run the S-, C-, X- complexes and the Q-type are considered, and the number of objects in each taxonomy is set with a pseudo-random number generator. We call the resulting color index distribution from each run the Random Probability Density Function, RPDF, to distinguish it from the PDF from our data. The process to generate each distribution is the same. The details of our MC simulation are as follows.

82 synthetic objects were used in each MC run in order to directly compare the RPDF with the PDF. From Mommert et al. (2016) and Erasmus et al. (2017), we expect the C- and S-type asteroids to be the main components of our sample, and to find a C/S ratio of ∼1. However, we take into account the possibility that our sample is composed of any combination of the taxonomic types con-

sidered. This is achieved by using a pseudo-random number generator under a uniform distribution with equal weights for the 3 complexes and the Q-type. The process to obtain the composition on each of the runs is as follows.

The order in which the number of elements is set for each complex and the Q type is randomly sorted. Each of them is labeled as n^{a}, n^{b}, n^{c} or n^{d}. The assignation of number of elements is always in alphabetical order, however the correspondence between the types and $n^{\mathrm{a-d}}$ is given by the pseudo random number generator. Then n^{a} can be assigned with any number between 0 and 82, the availability for n^{b} is 82-n^{a}, and similar for n^{c} and n^{d}.

The main subtypes of the complexes, respectively C-type, S-type and X-type, are the most likely to be present in our sample (Binzel et al. 2015). Therefore, in each of the random generated samples, half of the elements assigned to each complex are given to the main subtype, while the other half is uniformly distributed among the other subtypes (see Figure 1 for the r-i index of each of the members of these complexes). The number of elements in the second half will likely not be an integer multiple of the number of subtypes. For example, if 36 elements are assigned to the S-complex, 18 will correspond to the main type, the S-type. The remaining 18 will correspond to the other 4 subtypes of the complex, but 18 over 4 is not an integer. The procedure is therefore as follows: if the number of elements assigned to the 4 subtypes are $\mathbf{n}_{\mathrm{S1}}$, $\mathbf{n}_{\mathrm{S2}}$, $\mathbf{n}_{\mathrm{S3}}$, $\mathbf{n}_{\mathrm{S4}}$, then:

$\mathbf{n}_{\mathrm{S1}} = \mathrm{round}(18/4) = 5$; 18-5 = 13 elements available for the 3 other subtypes,

$\mathbf{n}_{\mathrm{S2}} = \mathrm{round}(13/3) = 4$; 13-4 = 9,

$\mathbf{n}_{\mathrm{S3}} = \mathrm{round}(9/2) \;\; = 5$; 9-5 = 4,

$\mathbf{n}_{\mathrm{S4}} = 4$.

In each run, the correspondence between the n_{S1-4} and the 4 subtypes is randomly sorted, so that over the 10^7 samples generated, none of the 4 subtypes is favored. The same criteria apply for the

C- and the X-complex. The main processes of the simulation are represented in Figure 5.

After applying all the selection criteria (see Section 4.4), some of the objects that were observed during different visits showed a different r-i index. This fact was not considered in the building of the RPDF. In the simulation, the elements that are not members of the C- or the S-complex are defined as "pollution".

Once the number of elements of each type in a single run is determined, it is necessary to add an error to them in order to emulate the photometric uncertainty. In order to take this into account, we fitted a Gaussian function to the distribution from Figure 2 and created a random distribution under that function. 82 errors from that distribution were assigned to the r-i indices of each of the determined types. This completes our generated sample. 82 elements were randomly selected following a distribution based on current NEOs observations. Each of the elements has an associated error, based on the error distribution of our observations. Having these, the RPDF was built up. After creating the 10^7 samples, the PDF was compared to each of the 10^7 RPDFs.

5. RESULTS

In order to extract the results from the simulations, we calculated the reduced χ^2 (χ^2_r) between the RPDF and the PDF. Since we are allowing the simulation to create any possible combination of the taxonomies considered, the χ^2_r range is wide as can be seen in Figure 7. We took the first percentile of simulations in terms of the χ^2_r. This is a set of 88 simulations ($\sim 10^{-5}$ from the total). The difference in χ^2_r between the best and the second to the best case is minimal. Both present 36 elements of the S-type, the first one suggest 38 C-types, while the second 39. The main difference is in the number of X- and Q-type objects. To analyze the behavior of the best cases we calculated the distribution of the ratio C/S, which is shown in Figure 8. Our best case corresponds to a value of 1.06 in this space. Notice that value is well within 1 standard deviation from the mean, but not in the bin where mean of the distribution is. We ascribe this to the fact the histogram is skewed
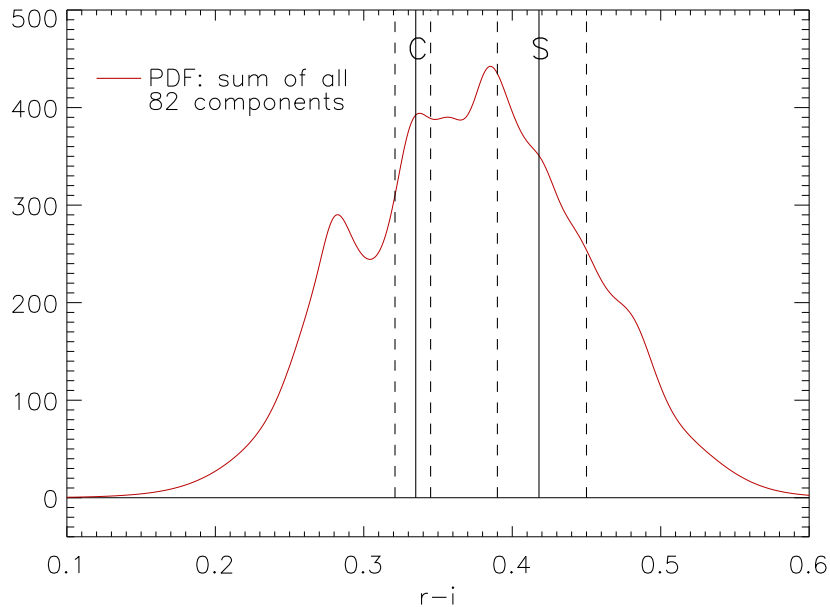
Figure 4. Probability Density Function of the color in our sample. Every visit is considered as a Gaussian centered in the color index obtained. Vertical lines represent the limits of the C and S complexes. See text for full explanation.

to the left, which is discussed in the next Section. Table 4 shows the percent compositions of the 4 taxonomic types considered according to our best case. The errors correspond to the standard deviation of the individual distribution of each class within the 1st percentile. Although we present results on the 3 complexes and the Q-type, the scope of this analysis is restricted to suggest a C/S ratio. All of our targets have a subkilometer diameter. We don't report subdivisions in size since there was not a clear trend on the results by doing so.

6. DISCUSSION

6.1. *Limitations and comparison with previous studies*

The strongest bias in our sample is the one presented by albedo. Our rapid-response approach is based on optically discovered objects, hence the sample targets are more likely to have moderate to high surface albedos. This can lead to an over-estimated fraction of S objects, which means the real fraction of C/S can be higher than the estimated here. Hence, our sample is biased, and although
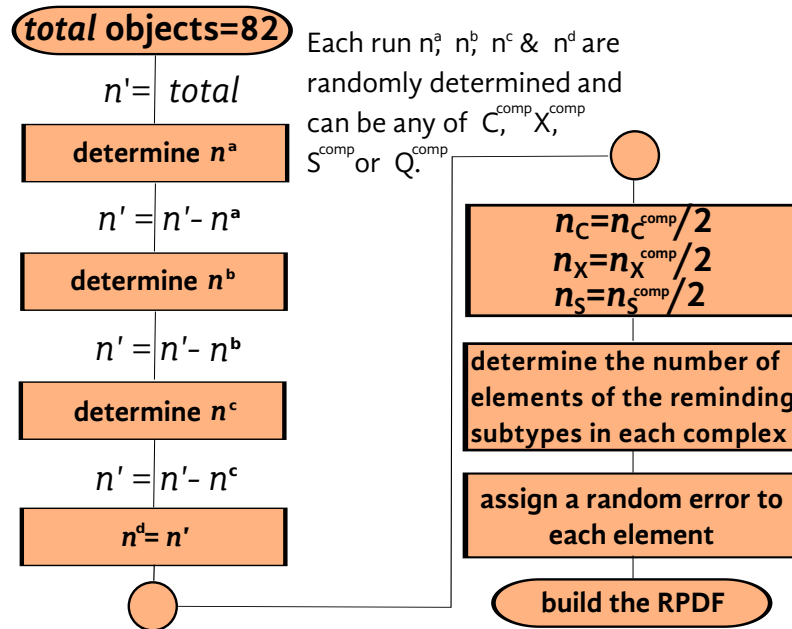
Figure 5. Main processes in the Monte Carlo simulation. Particularly the procedure for setting the number of objects of each type in the synthetic sample. Every box including the word "determine" involves a random process. n is the number of objects of a certain type or complex in a single run; the subindex indicates the referred taxonomy. Since there are C-, S- and X- complexes, as well as a C-, S- and X-types, a super index "comp" indicates when the variable is associated to the complex. n' is the number of objects available for the unassigned taxonomies at a certain point.

Taxonomic type	Percentage
C	46 ± 9
S	44 ± 8
X	8 ± 9
Q	2 ± 8

Table 4. Compositional fractions found in our Monte Carlo simulation.
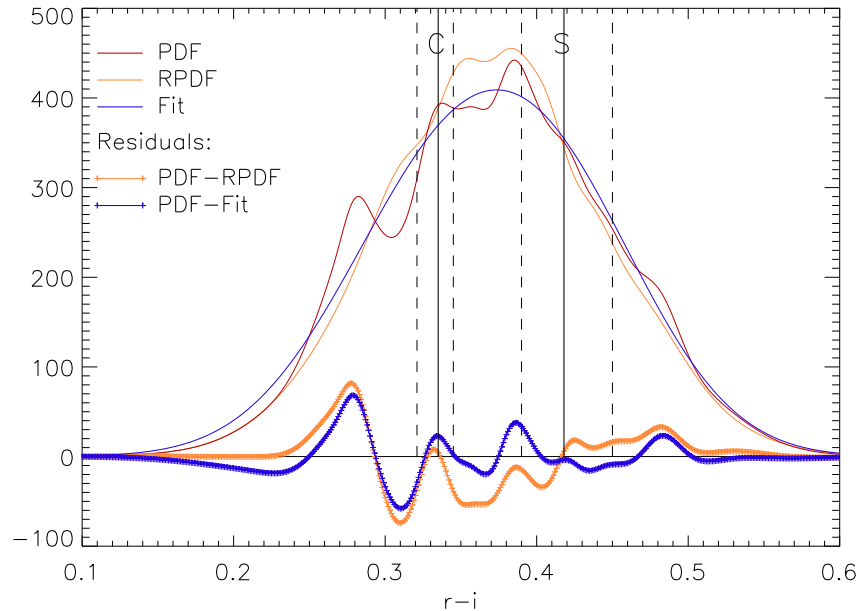
Figure 6. Probability Density Function (red) of the color in our sample. Equivalent to Figure 4, this time the best result from our MC simulation is overplotted (Random Probability Density Function, orange). A Gaussian fit to the PDF is also overplotted (blue). Both, the RPDF and the Fit make a good match with the data, as can be seen on the residuals (dashed orange and blue). See Sections 5 and 6.2 for details.

debiasing of NEOs had been carried out (Stuart & Binzel 2004; Hinkle et al. 2015) we will address it in a future work.

Our full sample contains observations in up to 6 different bands in the optical and near infrared range. However, the results presented here correspond to our control sample using only the r-i color. Hence, one the main goals of this article is to describe the methodology we are using for our observations. Our future work will include data in all bandpasses.

The distribution in Figure 8 is skewed to the left due to the feature at r-$i \sim 0.26 - 0.30$ in Figures 3 and 4. It is likely due to a systematic error in the observations causing a bluer color. The analysis of the complete sample will allow us to test this idea.
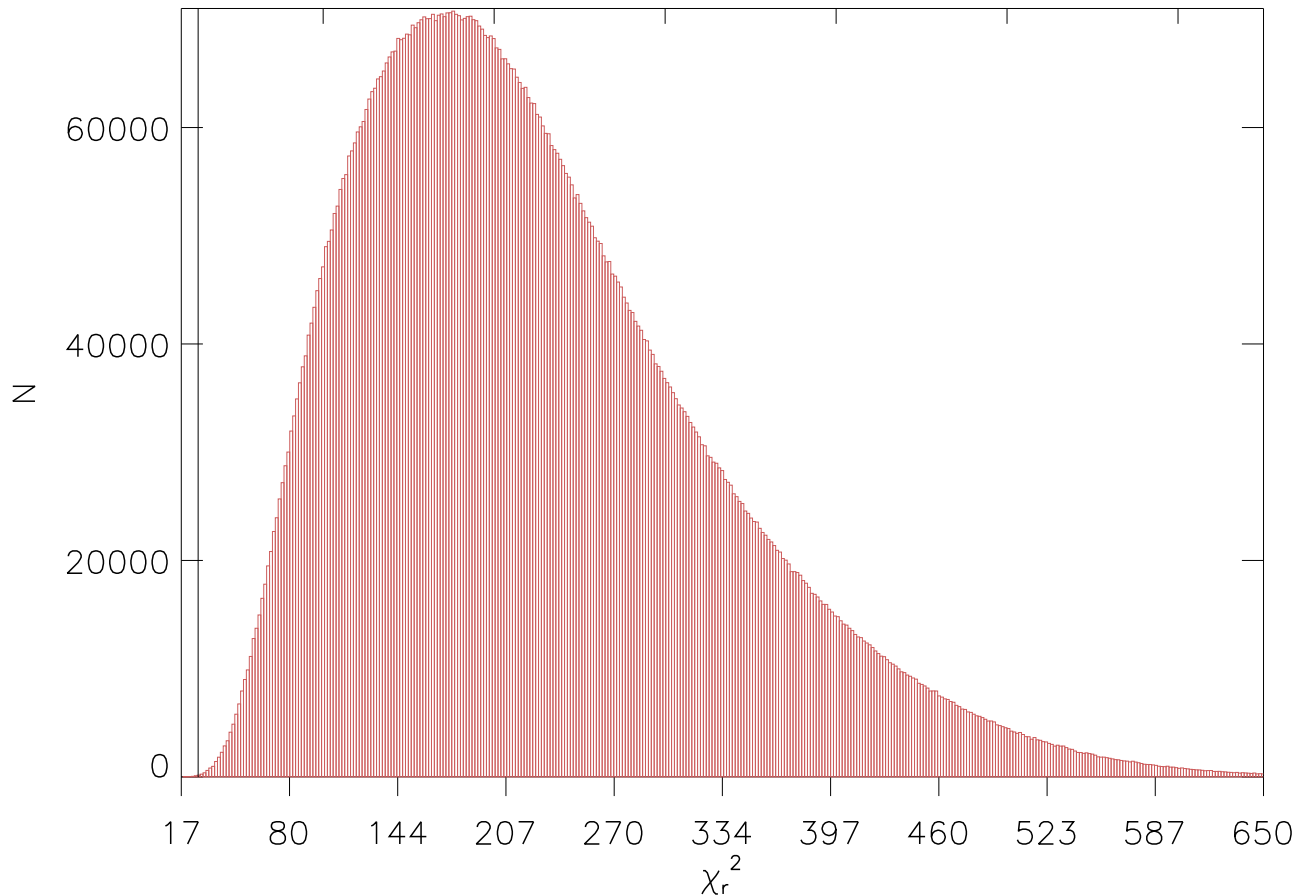
Figure 7. χ_r^2 from the 10^7 MC simulations. Vertical line shows the domain of the first percentile of simulations in terms of the χ_r^2.

Our full sample is one of the largest for small NEOs. The analysis of it as well as the work from other teams is needed for a comprehensive classification of this kind of objects. (As a comparison, Ivezić et al. (2001) made a study of the Main Belt including $\sim$ 13,000 objects). So far, the results from other teams on a similar size range to ours (subkilometer) are compared next. The fraction of S-type we find is in agreement within the error bars of the other studies. Ieva et al. (2018), from the analysis 67 NEOs found $\sim$ 61% of S-types. Lin et al. (2018), presents 51 subkilometer NEOs. With this sample they found an S fraction of $\sim$ 33%. Perna et al. (2018), for a sample of 146 objects, found an S fraction of $\sim$ 40%. Our team, using different telescopes and samples than the one presented in this paper, found $\sim$ 40% with 40 NEOs in Mommert et al. (2016), while Erasmus et al. (2017), with a sample of 45 objects, obtained an S fraction of $\sim$ 43%. Using a sample of 252 objects Stuart & Binzel
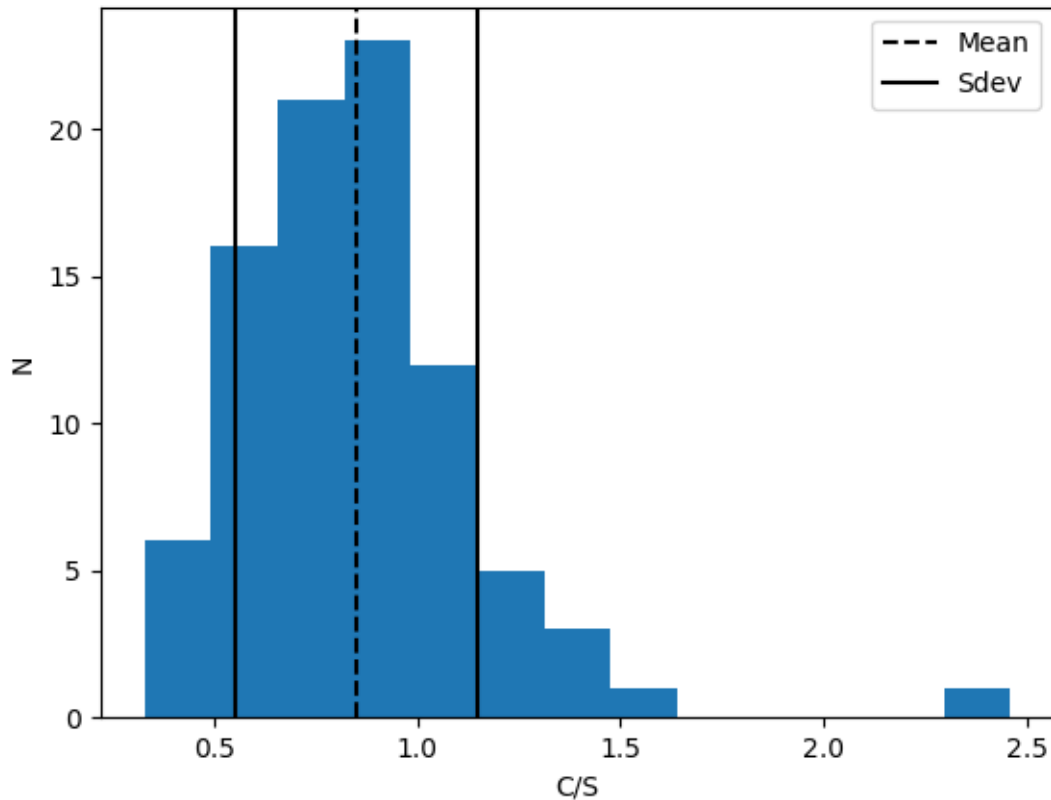
Figure 8. C/S distribution from the 1st percentile of our MC simulations in terms of χ_{r}^2. Note: the element in the far right is the 66th best fit, therefore not considered an issue but still considered in the estimation of the mean and standard deviation.

(2004) found an S-type fraction of 22%. This number is a reference for the distribution of NEOs, but is not directly comparable with our results since they performed bias correction, their sample includes Mars Crossing asteroids, and includes objects up to the 10 km scale. Binzel et al. (2018) (in press) uses a sample of 1040 objects, with a median of 0.7 km and finds an S fraction of $\sim 50\%$. The C-type fraction found in these same papers varies and can be as low as 10% vs the $\sim 46\%$ we suggest.

6.2. *Gaussian Fit*

With the purpose of getting a result independent from the MC simulation, we performed a Gaussian fit on the PDF, for which, we considered two components with fixed mean: one centered on the color

index of C-type asteroids (0.335), and the other one centered on the color index of S-type asteroids (0.418).

The result from our fit is overplotted to the PDF and RPDF in Figure 6. The two components of the fit are equivalent to 48% of S-type objects and 52% of C-type objects yielding $C/S = 1.07$, which is the same value than in the MC result. The residual (dashed blue in the figure) does not show a systematic behavior, and it is similar to the residual of subtracting the RPDF from the PDF (dashed yellow curve in the figure), so we assume this is primarily noise.

Fits considering other taxonomic types were made, yielding a larger residual. Because of this observation we decided only to consider the C- and S-type in the fitting process.

As can be seen in Figure 9, the width of both the C and S Gaussian distributions from our fit are wider than that of the PDF. This does not affect the result since we are using the ratio of the areas under the fits, but we explore different limits of integration on the abscissa axis for getting each of the areas:

(a) $[-\infty,\infty]$

(b) Integrating under the limits of the taxonomic types plus the maximum error allowed in color (0.075).

(c) $[-\infty,\mathrm{mid}_z]$ for the C Gaussian and $[\mathrm{mid}_z,\infty]$ for the S Gaussian.

where mid_z is the middle point between the r-i index of the C and S taxonomic complexes in terms of the z-score.
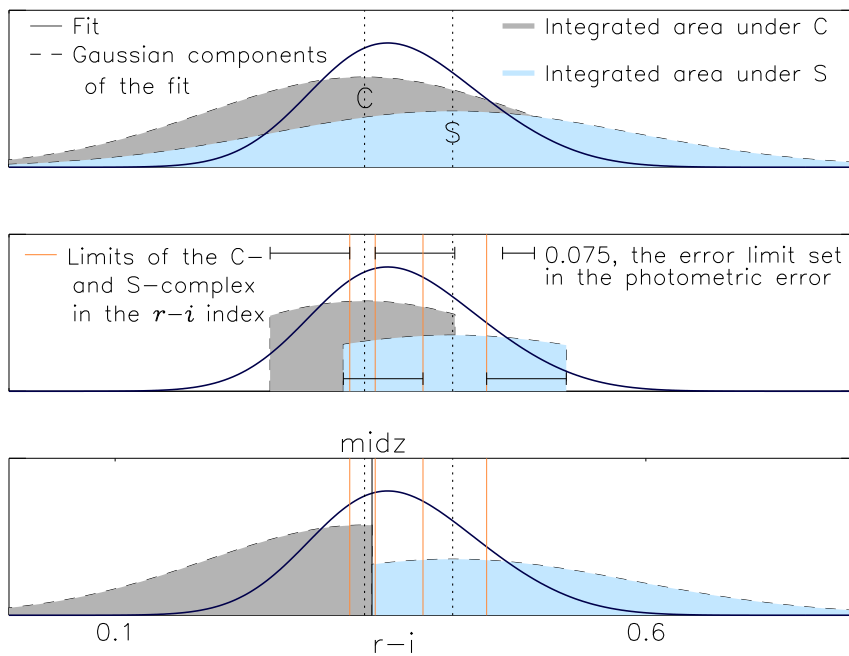
Figure 9. Integration limits considered for the Gaussian components of the fit. The fit is equivalent to the one showed in Figure 6. Vertical dotted shows the position of the main subtype of the C- and S-complex, thus the center of the Gaussian components. The width of the Gaussians is related to the error of the individual elements, the ordinate axis has no practical meaning. See text for more details.

The three integration limits are shown in Figure 9. They yield a similar C/S ratio, but, method (b) proved to be more stable as a function of the pollution in test runs of the MC[5] analysis. With the use of this method we made a cut in the tails of the Gaussians, obtaining more localized components. Notice from Figure 1 that the main types of the C- and S-complex are positioned nearly at the center of their corresponding complex range, making the integration reliable.

We explored the C/S ratio (obtained in Section 4.5) as a function of the upper error allowed in the clean sample. This dependence is shown in Figure 10. Excluding the extremes of the abscissa range on this plot, the C/S ratio does not present a strong dependence on the error limit. Additionally, more than **70**% of the objects that passed our other selection criteria have an error lower than 0.075

---

[5] We used Equations 3 - 5 presented in Section 6.3 to compare the results.
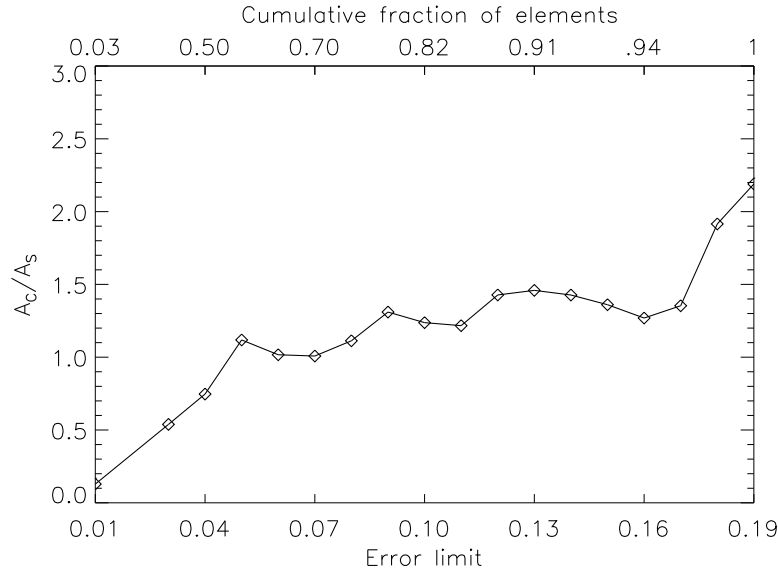
Figure 10. C-type to S-type ratio found with a Gaussian fit to the PDF after using different upper error selection criteria. Notice that this figure is a comparison of different error limits for our sample and it does not represent our main results.

(and most of the asteroids in our full sample too, see Figure 2).

6.3. *Accuracy*

The composition of the RPDF is generated during the simulation, therefore it is known per se. Hence, by applying a Gaussian fit to the RPDF, such as the one described in Section 4.5, we can obtain the reliability of the fit in a particular case with the relative error:

$$e = \frac{f_{\mathrm{m}} - f_{\mathrm{k}}}{f_{\mathrm{k}}}, \tag{3}$$

where f_{k} stands for the known compositional fraction of a certain type in the RPDF, and f_{m} for the fraction measured through the Gaussian fit. Then we can consider all of the instances of a fixed k in the 10^7 runs with:

$$\epsilon = \bar{e}, \tag{4}$$

and the spread of Equation 4 is measured with:

$$\sigma = \sqrt{\overline{e^2} - \overline{e}^2}.$$ (5)

Equations 3 -5 are identical for the three complexes and the Q-type.

As a general trend, ϵ was larger for the C complex than for the S one. This suggests that if objects of the X-complex and Q-type are present in the data sample, is more likely for them to be identified as members of the C-complex than the S-complex by performing a Gaussian fit. This was also observed in test runs where only the main type of each complex was used. In terms of the r-i index, the Q-type is closer to the C-complex, while the X-complex is closer to the S (see Figure 1). It is possible that this behavior is due to the relative width of the C- and S-complexes and not to the position of the X-complex itself.

The errors reported in Table 4 were obtained by taking the standard deviation of each complex/type from the set of 12 best matches from the MC simulation described in previous subsection.

The Gaussian fit is not as robust as the MC analysis for obtaining the results, therefore we can expect lower accuracy. Having a fit centered on the C and S taxonomic components, the ratio of the area under the corresponding Gaussians is directly related to the compositional fraction of the sample. The fraction of S-type elements obtained through a Gaussian fit is more reliable than the C-type one. For this reason, from the fit we focus on the S-type fraction obtained: 48%, which within the error bars is compatible with our MC result.

Although in our simulations we allowed for a wide range of variation in the randomly generated sample, our results partially rely on the assumptions described in Section 4.6.

7. CONCLUSIONS AND FUTURE OUTLOOK

With the use of spectrophotometry on a 1.5 m robotic telescope, we performed rapid-response observations of small Near Earth Objects. Here we present the results from our optical sample. Measurements were simultaneously made in the r and i band. After applying selection criteria, our sample consisted on 131 observations of 82 different NEOs within the size range of ~30-850m.

For the size range considered, we found that C-type asteroids are same as frequent than the S-type, finding C/S = 1.06. Together, these two asteroid types represent $\sim 90\%$ of our sample, with the rest likely to be Q- and X-type asteroids. This compositional fraction is in agreement with the results of our previous publications (Mommert et al. 2016; Erasmus et al. 2017) which are based on UKIRT and KMTNet-SAAO observations.

Observations from our program are ongoing. The facility used in this study is now observing with the Z, Y, J and H near infrared bands in addition to the optical r and i. By analyzing the data set presented here, we created the tools to analyze the observations from the rest of the campaign (2016-ongoing). Future publications from this study will include observations from multiple photometric bands, which will improve the accuracy of the results.

8. ACKNOWLEDGMENTS

REFERENCES

Becerra, R. L., Watson, A. M., Lee, W. H., et al. 2017, ApJ, 837, 116

Binzel, R. P., Reddy, V., & Dunn, T. L. 2015, Asteroids IV, 243

R.P. Binzel and F.E. DeMeo and S.J. Bus and A. Tokunaga and T.H. Burbine and C. Lantz and D. Polishook and B. Carry and A. Morbidelli and M. Birlan and P. Vernazza and B.J. Burt and N. Moskovitz and S.M. Slivan and C.A. Thomas and A.S. Rivkin and M.D. Hicks and T. Dunn and V. Reddy and J.A. Sanchez and M. Granvik and T. Kohout 2018, Icarus

Brown, P. G., Assink, J. D., Astiz, L., et al. 2013, Nature, 503, 238

Butler, N., Klein, C., Fox, O., et al. 2012, Proc. SPIE, 8446, 844610

Butler, N., Watson, A. M., Kutyrev, A., et al. 2017, GRB Coordinates Network, Circular Service, No. 21915, #1 (2017), 21915, 1

Butler, N., Watson, A. M., Kutyrev, A., et al. 2017, GRB Coordinates Network, Circular Service, No. 22061, #1-2018 (2017), 22061, 1

Butler, N., Watson, A. M., Kutyrev, A., et al. 2017, GRB Coordinates Network, Circular Service, No. 22182, #1 (2017), 22182, 1

Carry, B., Solano, E., Eggl, S., & DeMeo, F. E. 2016, Icarus, 268, 340

Carvano, J. M., Hasselmann, P. H., Lazzaro, D., & Mothé-Diniz, T. 2010, A&A, 510, A43

DeMeo, F. E., Binzel, R. P., Slivan, S. M., & Bus, S. J. 2009, Icarus, 202, 160

Delsemme, A. H. 1991, IAU Colloq. 116: Comets in the post-Halley era, 167, 377

Erasmus, N., Mommert, M., Trilling, D. E., et al. 2017, AJ, 154, 162

Ieva, S., Dotto, E., Epifani, E. M., et al. 2018, A&A, 615, A127

Galache, J. L., Beeson, C. L., McLeod, K. K., & Elvis, M. 2015, Planet. Space Sci., 111, 155

García-Díaz, M. T., González-Buitrago, D., López, J. A., et al. 2014, AJ, 148, 57

Giorgini, J. D., Yeomans, D. K., Chamberlin, A. B., et al. 1997, BAAS, 29, 1099

Hinkle, M. L., Moskovitz, N., Trilling, D., et al. 2015, AAS/Division for Planetary Sciences Meeting Abstracts #47, 47, 301.04

Ivezić, Ž., Tabachnik, S., Rafikov, R., et al. 2001, AJ, 122, 2749

Littlejohns, O. M., Butler, N. R., Cucchiara, A., et al. 2015, MNRAS, 449, 2919

Lin, C.-H., Ip, W.-H., Lin, Z.-Y., et al. 2018, Planet. Space Sci., 152, 116

Malhotra, R. 1997, Bulletin of the American Astronomical Society, 29, 23.02

McAdam, M. M., Sunshine, J. M., Howard, K. T., et al. 2018, Lunar and Planetary Science Conference, 49, 2081

Mommert, M., Trilling, D. E., Borth, D., et al. 2016, AJ, 151, 98

Moskovitz, N., Thirouin, A., Binzel, R., et al. 2015, IAU General Assembly, 22, 2255616

Popescu, M., Perna, D., Barucci, M. A., et al. 2018, MNRAS, 477, 2786

Ricci, D., Ramón-Fox, F. G., Ayala-Loera, C., et al. 2015, PASP, 127, 143

Stuart, J. S., & Binzel, R. P. 2004, Icarus, 170, 295

Perna, D., Barucci, M. A., Fulchignoni, M., et al. 2018, Planet. Space Sci., 157, 82

Ryan, E. L., Mizuno, D. R., Shenoy, S. S., et al. 2015, A&A, 578, A42

Tapia, M., Rodríguez, L. F., Tovmassian, G., et al. 2014, RMxAA, 50, 127

Taylor, John R. 1997, An introduction to error analysis, 2nd Ed, p. 176

Thomas, C. A., Trilling, D. E., Emery, J. P., et al. 2011, AJ, 142, 85

Thomas, C. A., Emery, J. P., Trilling, D. E., et al. 2014, Icarus, 228, 217

Watson, A. M., Richer, M. G., Bloom, J. S., et al. 2012, Proc. SPIE, 8444, 84445L

Warner, B. D., Harris, A. W., & Pravec, P. 2009, Icarus, 202, 134

All Authors and Affiliations

S. Navarro-Meza,[1,2] M. Mommert,[3,2] D.E. Trilling,[2] N. Butler,[4,5] M. Reyes-Ruiz,[1]
B. Pichardo,[6] T. Axelrod,[7] R. Jedicke,[8] and N. Moskovitz[3]

[1] *Instituto de Astronomía, Universidad Nacional Autónoma de México, Ensenada B.C. 22860, México.*

[2] *Department of Physics and Astronomy, Northern Arizona University, Flagstaff, AZ 86001, USA*

[3] *Lowell Observatory, Flagstaff, AZ 86001, USA*

[4] *School of Earth and Space exploration, Arizona State University, Tempe, AZ 85287, USA*

[5] *Cosmology Initiative, Arizona State University, Tempe, AZ 85287, USA*

[6] *Instituto de Astronomía, Universidad Nacional Autónoma de México, Ciudad Universitaria, D.F. 04510, México.*

[7] *Steward Observatory, University of Arizona, Tucson, AZ 85721, USA*

[8] *Institute for Astronomy, University of Hawaii at Manoa, Honolulu, HI 96822, USA*